

Spectral tuning and nanoscale localization of single color centers in silicon via controllable strain

Buzzi, Alessandro; Papon, Camille; Pirro, Matteo; Hooybergs, Odiel; Raniwala, Hamza; Saggio, Valeria; Errando-Herranz, Carlos; Englund, Dirk

DOI

[10.1038/s41467-025-63871-8](https://doi.org/10.1038/s41467-025-63871-8)

Publication date

2025

Document Version

Final published version

Published in

Nature Communications

Citation (APA)

Buzzi, A., Papon, C., Pirro, M., Hooybergs, O., Raniwala, H., Saggio, V., Errando-Herranz, C., & Englund, D. (2025). Spectral tuning and nanoscale localization of single color centers in silicon via controllable strain. *Nature Communications*, 16(1), Article 8829. <https://doi.org/10.1038/s41467-025-63871-8>

Important note

To cite this publication, please use the final published version (if applicable).
Please check the document version above.

Copyright

Other than for strictly personal use, it is not permitted to download, forward or distribute the text or part of it, without the consent of the author(s) and/or copyright holder(s), unless the work is under an open content license such as Creative Commons.

Takedown policy

Please contact us and provide details if you believe this document breaches copyrights.
We will remove access to the work immediately and investigate your claim.

Spectral tuning and nanoscale localization of single color centers in silicon via controllable strain

Received: 12 April 2025

Accepted: 31 August 2025

Published online: 03 October 2025

 Check for updates

Alessandro Buzzi^{1,4}✉, Camille Papon^{1,4}✉, Matteo Pirro^{2,3}, Odiel Hooybergs¹, Hamza Raniwala¹, Valeria Saggio¹, Carlos Errando-Herranz^{2,3}✉ & Dirk Englund¹✉

The development of color centers in silicon enables scalable quantum technologies by combining telecom-wavelength emission and compatibility with mature silicon fabrication. However, large-scale integration requires precise control of each emitter's optical transition to generate indistinguishable photons for quantum networking. Here, we demonstrate a foundry-fabricated photonic integrated circuit (PIC) combining suspended silicon waveguides with a microelectromechanical (MEMS) cantilever to apply local strain and spectrally tune individual G-centers. Applying up to 35 V between the cantilever and the substrate induces a reversible wavelength shift of the zero-phonon line exceeding 100 pm, with no loss in brightness. Moreover, by modeling the strain-induced shifts with a digital twin physical model, we achieve vertical localization of color centers with sub-3 nm vertical resolution, directly correlating their spatial position, dipole orientation, and spectral behavior. This method enables on-demand, low-power control of emission spectrum and nanoscale localization of color centers, advancing quantum networks on a foundry-compatible platform.

Color centers are solid-state spin-photon interfaces that serve as core components for quantum information processing^{1,2}. Their long spin and optical coherence times, combined with the ability to be optically initialized and read out, make them suitable for quantum communication^{3–5}, simulation⁶, and computing applications⁷. Silicon photonics as a host platform for color centers, such as G-centers⁸ and T-centers⁹, offers a scalable solution for quantum technologies at telecom wavelengths, driven by advanced fabrication techniques and seamless integration with photonic active components and CMOS electronics¹⁰. Integration of these color centers into photonic structures, such as cavities^{11–14} and waveguides^{15–17}, has demonstrated their potential as a scalable quantum photonic platform¹⁸.

The generation of large-scale entangled states is fundamental to the advancement of quantum platforms^{19,20}. Realizing such states within solid-state quantum emitters requires the reliable generation of indistinguishable photons. The scale and fidelity of the entangled state ultimately depend on the ability to discriminate individual color centers and control their emission wavelength to overcome the sensitivity of their properties from the local strain and charge environment^{20–23}. Recent studies have investigated the influence of strain^{24,25}, electric fields^{26,27}, and laser irradiation¹⁶ on color centers in silicon, uncovering fundamental properties and viable spectral tuning mechanisms. In particular, strain tuning has emerged as a highly effective approach for controllably shifting the optical transition energies of diamond color centers, enabling reversible wavelength alignment between otherwise

¹Research Laboratory of Electronics, Massachusetts Institute of Technology, Cambridge, MA, USA. ²QuTech and Kavli Institute of Nanoscience, Delft University of Technology, Delft, The Netherlands. ³Department of Quantum and Computer Engineering, Delft University of Technology, Delft, The Netherlands.

⁴These authors contributed equally: Alessandro Buzzi, Camille Papon. ✉e-mail: abuzzi@mit.edu; cpapon@mit.edu; c.errandoherranz@tudelft.nl; englund@mit.edu

non-identical emitters^{28–31}. Despite these advances, the inability to independently tune the emission spectrum of individual color centers in silicon and discriminate them based on their tuning behaviors limits the scalability and performance of the platform.

Here, we address these challenges by demonstrating reversible spectral tuning and nanoscale localization of individual G-centers in photonic circuits through local strain control. Using a suspended waveguide cantilever actuated via Micro-Electro-Mechanical System (MEMS) mechanisms, we observe hysteresis-free tuning of emission wavelengths via low-power strain control. Additionally, by modeling the spectral tuning through the piezospectroscopic model, the electromechanical behavior of the device, and the emitter's collection efficiency, we extract the color center's orientation and vertical position with nanometric resolution.

Results

Device concept and design

The device's working principle, illustrated in Fig. 1, involves controlling strain within a suspended silicon waveguide to modulate the emission wavelength of embedded G-centers (Fig. 1a). The MEMS consists of a mechanical cantilever capacitively actuated by a voltage difference between the silicon device layer and the silicon handle (Fig. 1b). The applied voltage induces strain along the waveguide, which affects the energy levels of the G-centers (Fig. 1c), resulting in a shift in their emission wavelength (Fig. 1d).

An above-bandgap laser excites the G-centers via a confocal microscope focused on the cantilever. Emission from the color centers is collected through the waveguide, which is suspended by mechanical tethers. A photonic Bragg reflector at the end of the waveguide reflects the emission along the cantilever, increasing the collection efficiency. A linear inverse taper then couples the emitted light out, which is collected by an ultra-high numerical aperture (UHNA) fiber and detected by a superconducting nanowire single-photon detector

(SNSPD). The photonic components were optimized for the fundamental quasi-TE waveguide mode using finite-difference time-domain (FDTD) simulations. Further details on the design and experimental setup can be found in Supplementary Notes 1 and 2.

Foundry-based fabrication

The fabrication process consists of three main phases: preprocessing, commercial fabrication, and post-processing.

During preprocessing, we start with a 100-oriented silicon-on-insulator (SOI) wafer. The SOI device layer is 220 nm thick, and the bottom oxide is 2 μm thick. Carbon ion implantation into the device layer is followed by rapid thermal annealing (RTA) to form G-centers.

In the commercial fabrication phase, the wafer is sent to a photonics foundry for electron beam lithography patterning and reactive ion etching (RIE) of the device layer. A 2 μm silicon dioxide cladding is deposited via plasma-enhanced chemical vapor deposition (PECVD).

Post-processing involves releasing the MEMS structures by wet etching in hydrofluoric acid (HF), removing the oxide cladding, and undercutting the structures. Critical point drying (CPD) is used to prevent collapse during drying. Chromium-gold electrical contact pads are patterned through electron beam evaporation with a shadow mask to avoid any liftoff or etching step that could damage the suspended structures (see Supplementary Note 3). Finally, the chip is wire-bonded to a printed circuit board for electrical connection. The details of the fabrication process are provided in the "Methods" section.

Schematics of the fabrication process and final device are shown in Fig. 2a, b. Scanning electron micrographs of the key photonic components after fabrication are shown in Fig. 2c, d. Figure 2c displays the MEMS cantilever waveguide, including the Bragg reflector and tethers. Figure 2d shows the linear inverse taper edge coupler. The Bragg reflector is designed with a reflectance of 95%. The tether transmission, measured experimentally, is 94%, and the coupling efficiency of the edge coupler to the UHNA fiber is calculated to be above

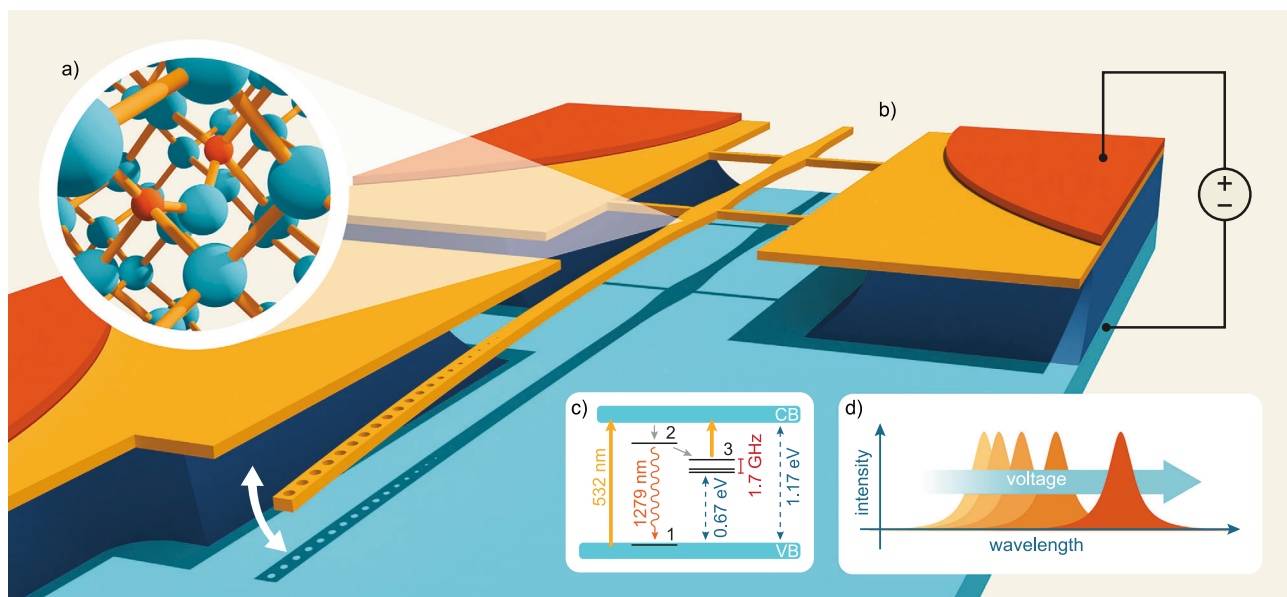


Fig. 1 | Illustration of the MEMS cantilever for strain tuning of color centers. **a** Ball-and-stick model of the G-center, a color center in silicon, comprising two substitutional carbon atoms (orange) and an interstitial silicon atom (light blue) within the silicon crystal lattice. **b** Illustration of the suspended cantilever waveguide, held in place by tethers that also provide electrical contact, and terminated by a Bragg reflector. The waveguide can be bent through capacitive actuation by applying a voltage difference between the waveguide and the silicon handle ground plane. This controlled bending enables accurate manipulation of strain within the cantilever. **c** Schematic of the silicon conduction-band minimum (CB) and valence-band maximum (VB), overlaid with the G-center energy levels. 1. denotes the

electronic ground state, 2. the optically excited state, and 3. the three sub-levels of the metastable triplet ($S=1$). The zero-field splitting of the triplet is derived from ref. 50, while its energy from the ground state is obtained from ref. 34. The diagram shows the above-band excitation and the radiative and non-radiative transitions of the color center, which are influenced by the strain introduced by the cantilever actuation. **d** Conceptual plot of the G-center emission spectrum, displaying intensity as a function of wavelength. The plot shows how strain shifts the emission spectrum. The magnitude of this shift is influenced by the emitter's orientation and position within and along the cantilever.

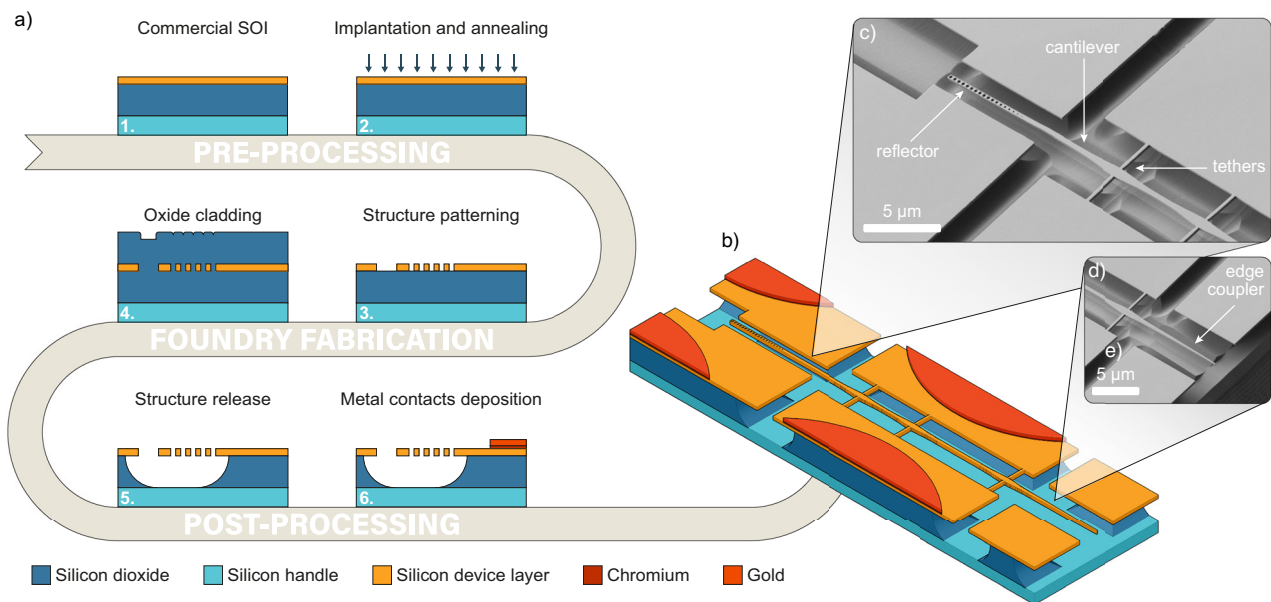


Fig. 2 | Device fabrication process and micrographs. **a** Fabrication starts with a commercial silicon-on-insulator (SOI) chip (1). The chip undergoes carbon ion implantation followed by annealing to restore the crystalline structure and form G-centers (2). The chip is then sent to a photonics foundry for device layer etching (3) and oxide cladding deposition (4). In the final post-processing steps, MEMS structures are released via undercutting in wet etching, followed by critical point drying (5). Electrical contacts are deposited by metal evaporation through a shadow mask aligned with the pad area (6). **b** Isometric schematic of the fabricated device,

showing the cantilever terminated by a Bragg reflector at the top and an edge coupler at the bottom. The central part of the device, illustrating three of the actual ten tethers, has been shortened in this view for clarity. **c** Micrograph of the suspended MEMS cantilever. **d** Micrograph of the linear inverse taper edge coupler. The micrographs were acquired from an equivalent device; the actual strain-tuning device was not imaged via scanning electron microscopy to avoid structural collapse due to stray charging.

12%. Further details on the efficiency of the device's components are provided in Supplementary Note 4.

Spectral tuning of single G-centers

After packaging, the device is mounted in a closed-cycle cryostat and cooled down to cryogenic temperatures ($T = 7$ K) to investigate photoemission from waveguide-coupled G-centers. An above-band continuous-wave laser ($\lambda_{\text{exc}} = 532$ nm, see Supplementary Note 5 for additional above-band spectroscopy) is scanned around the suspended cantilever region, and emission from G-centers is collected into UHNA fibers through the tapered edge coupler. The UHNA fibers are then spliced to SMF28 fibers for further routing (see Supplementary Note 6). The color center photoluminescence (PL) is then coupled to a free-space bandpass filter (1250–1300 nm) to suppress the excitation laser and unwanted background emission before detection on the SNSPDs (see “Methods”). The PL raster scan shown in Fig. 3a reveals two bright locations (*A* and *B*) in the cantilever part of the device (see inset of Fig. 3a). The unfiltered emission from the two locations is then sent to a spectrometer with a resolution of 40 pm (see “Methods”) and reveals several zero-phonon lines (ZPLs), as shown in Fig. 3b. On each excitation position, we record the spectra of the ZPLs as a function of the applied voltage between the cantilever and the substrate. As the voltage is increased from 0 V up to 35 V, the central wavelength of the ZPL shifts, with a sign and magnitude analyzed in the theoretical model introduced in the next section. A maximum tuning of $\delta = 130$ pm is observed, with an electrical power dissipated as low as ≈ 10 nW (see Supplementary Note 5), and we ensure that the process is reversible by recording spectra from 35 V back to 0 V, as shown in Supplementary Note 5. This actuation results in a spectral tuning rate of 680 MHz/V, and other devices investigated, as shown in Supplementary Note 7, demonstrate that rates up to 5.8 GHz/V are achievable. This latter result, obtained by applying a strain with a combination of lateral and vertical displacement, is sufficient to bring two emitters in resonance (see Supplementary Note 7).

To verify the two-level system nature of the tunable ZPLs, we first investigate the saturation of the single ZPL on position *B* by increasing the excitation laser power and recording individual spectra on the spectrometer. The integrated intensity of each peak as a function of excitation power is fitted to the saturation of a two-level system (see “Methods”) from which we extract a saturation power of $P_{\text{sat}} = (13.6 \pm 0.5) \mu\text{W}$ measured before the objective, as shown in Fig. 3c. Saturation curves from other emitters are provided in Supplementary Note 5, all demonstrating agreement with a model of saturation of a two-level system.

We then verify the single-photon nature of the collected PL by performing a Hanbury-Brown-Twiss experiment on the narrow-filtered ZPL (see “Methods”) from position *B* at saturation. Figure 3d shows the time correlation between two SNSPDs, measured after the ZPL emission is split using a 50:50 fiber beam splitter, with a bin size of 700 ps. We measure a second-order correlation function of $g^{(2)}(0) = 0.09 \pm 0.04$ without background subtraction and after normalization by long-time delay correlation (200 μs), a clear signature of emission from a single emitter. Deviation from the ideal second-order correlation of a pure single-photon source $g^{(2)}(0) = 0$ is attributed to residual background emission or emission from other G-centers. The error bars on each correlation, and thus on the raw measured $g^{(2)}(0)$, are given by Poissonian statistics. The raw correlations are fitted to a second-order correlation function, which includes a bunching term³² due to blinking to phenomenological dark states³³ or to the dark metastable triplet state identified in G-centers³⁴. We extract an antibunching time constant of $\tau_a = 2.7 \pm 0.5$ ns while the bunching time constant reads $\tau_b = 6.0 \pm 0.8$ ns. We measure the color center's lifetime by time-resolved measurement of PL from the ZPL excited at position *A* with an above-band pulsed laser ($\lambda_{\text{exc}} = 532$ nm) while filtering the A2 line. The result is shown in Fig. 3e and is fitted to a mono-exponential decay, giving a lifetime of $\tau = 6.61 \pm 0.09$ ns. A similar result, shown in Supplementary Note 5, is obtained for ZPL on position *B*, indicating a

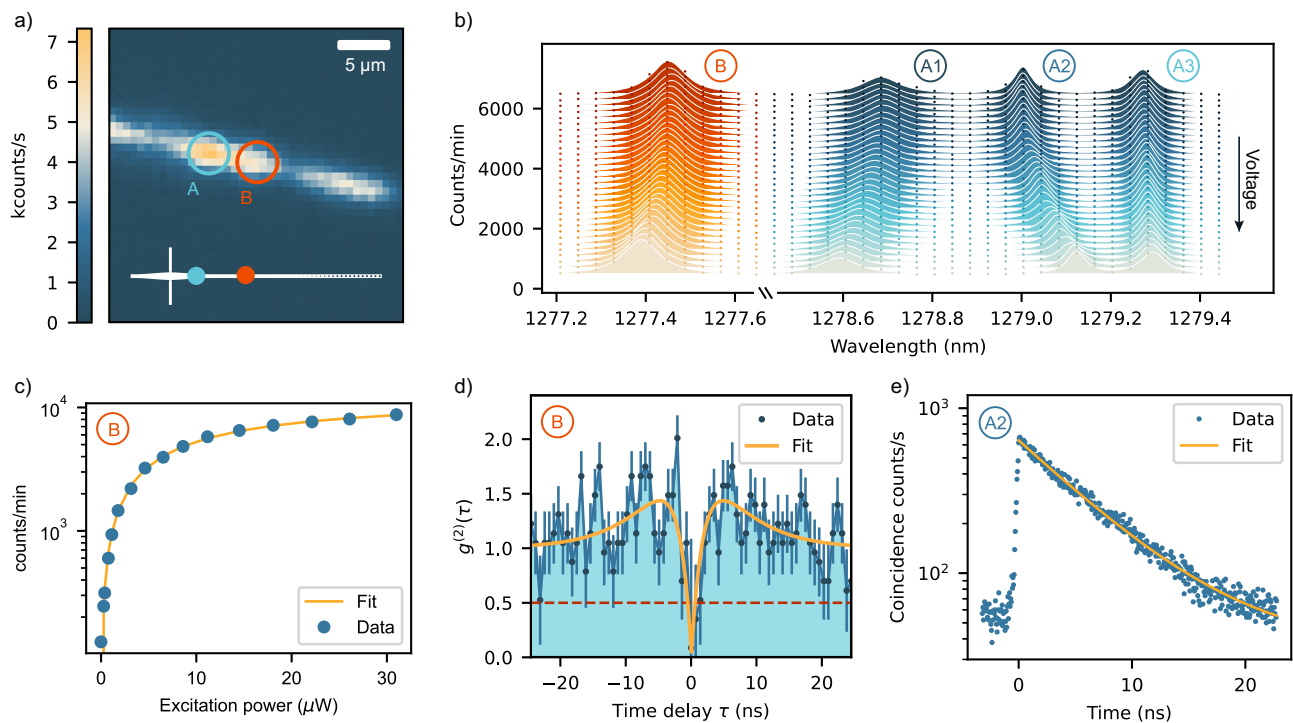


Fig. 3 | Strain tuning of single waveguide-coupled G-centers.

a Photoluminescence (PL) emitted from waveguide-coupled G-centers collected from the edge coupler and detected with SNSPDs, as a function of the excitation laser position ($\lambda_{\text{exc}} = 532 \text{ nm}$). The PL is filtered with a broadband free-space bandpass filter (1250–1300 nm). Two G-center spots within the waveguide are identified as *A* and *B* and are sketched in the inset. **b** Several zero-phonon lines are observed on the spectrometer at locations *A* (blue) and *B* (orange). The central wavelengths shift with the applied DC voltage. The white lines indicate the Lorentzian fit. **c** Integrated intensity on the spectrometer as a function of excitation power on emitter *B*. The yellow line indicates the fit to power saturation of a two-

level system, from which we extract a saturation power of $P_{\text{sat}} = (13.6 \pm 0.5) \mu\text{W}$. **d** Second-order correlation function of the filtered zero-phonon line shown in (c), excited in continuous-wave at saturation, with a measured $g^{(2)}(0) = 0.09 \pm 0.04$. The yellow line represents a fit to a three-level system, including a dark state, which gives rise to antibunching and bunching timescales. The dashed orange line indicates the threshold below which emission from a single emitter is demonstrated. **e** Time-resolved measurement of the zero-phonon line A_2 under pulsed above-band excitation, close to saturation. The lifetime extracted from a mono-exponential decay, $\tau = (6.61 \pm 0.09) \text{ ns}$, is typical of G-centers.

lifetime of $\tau = 6.4 \pm 0.1 \text{ ns}$. We highlight that previous works demonstrated that the lifetime is independent of the pulsed excitation power^{11,16}. The lifetime value confirms that the color centers employed in this work are the genuine G-centers^{11,35}, which is guaranteed by following a similar implantation process as in refs. 11,16. Additional spectroscopy results for each investigated ZPL are available in Supplementary Note 5.

Model-assisted nanoscale localization

The spectral response of the emitters to the mechanical actuation depends on two microscopic characteristics: the color centers' position inside the waveguide and their orientation within the crystalline lattice. The position influences the magnitude of strain applied to them, while the orientation of the defect determines how sensitive they are to the applied strain. Additionally, both characteristics affect the coupling efficiency of the emitter to the waveguide mode. By modeling these factors, we can extract the color centers' defect orientation and vertical position with nanometric resolution.

To estimate the position and orientation of the emitters, we express the joint probability conditioned on the orientations of the emitters. The variables Z_i represent the emitters' vertical positions relative to the waveguide's center, while O_i denotes the equivalence classes of their orientations. The equivalence classes of orientations, O_i , group together orientations that exhibit identical behaviors for strain, such as having the same piezospectroscopic coefficients^{36,37}, and dipole orientation, meaning they couple with the same efficiency into the fundamental quasi-TE waveguide mode. To collectively represent all emitters, we define $E = \{A_1, A_2, A_3, B\}$, with $Z_E = \{Z_i; i \in E\}$ as

their positions and $O_E = \{O_i; i \in E\}$ as their orientations. The joint probability of emitter positions and orientations is

$$P(Z_E \cap O_E) = P(Z_E | O_E) P(O_E), \quad (1)$$

assuming the marginal independence of emitter positions given their orientations allows us to factorize the joint probability of all vertical positions. Substituting this factorization into the original expression gives

$$P(Z_E \cap O_E) = \left(\prod_{i \in E} P(Z_i | O_i) \right) P(O_E). \quad (2)$$

Here, $P(O_E)$ represents the joint probability distribution of the emitters' orientation equivalence classes, which cannot be factorized due to the model's interdependence between the estimated emitter orientations. The intensities of the observed emitters provide information about their coupling efficiencies, which, in turn, influence the estimation of the other emitters' coupling efficiencies and dipole orientations.

The model used to determine each scenario's probability is shown in Fig. 4a, with the probability distribution of the emitters' vertical position presented in the right plot of Fig. 4b. We estimate the probability by evaluating the likelihood of all emitter orientation and vertical position combinations, starting with the product of conditional probabilities for each emitter's position given its dipole orientation. The coordinate system used for the model is illustrated in Fig. 4c. The origin of the coordinate system is defined at the center of the

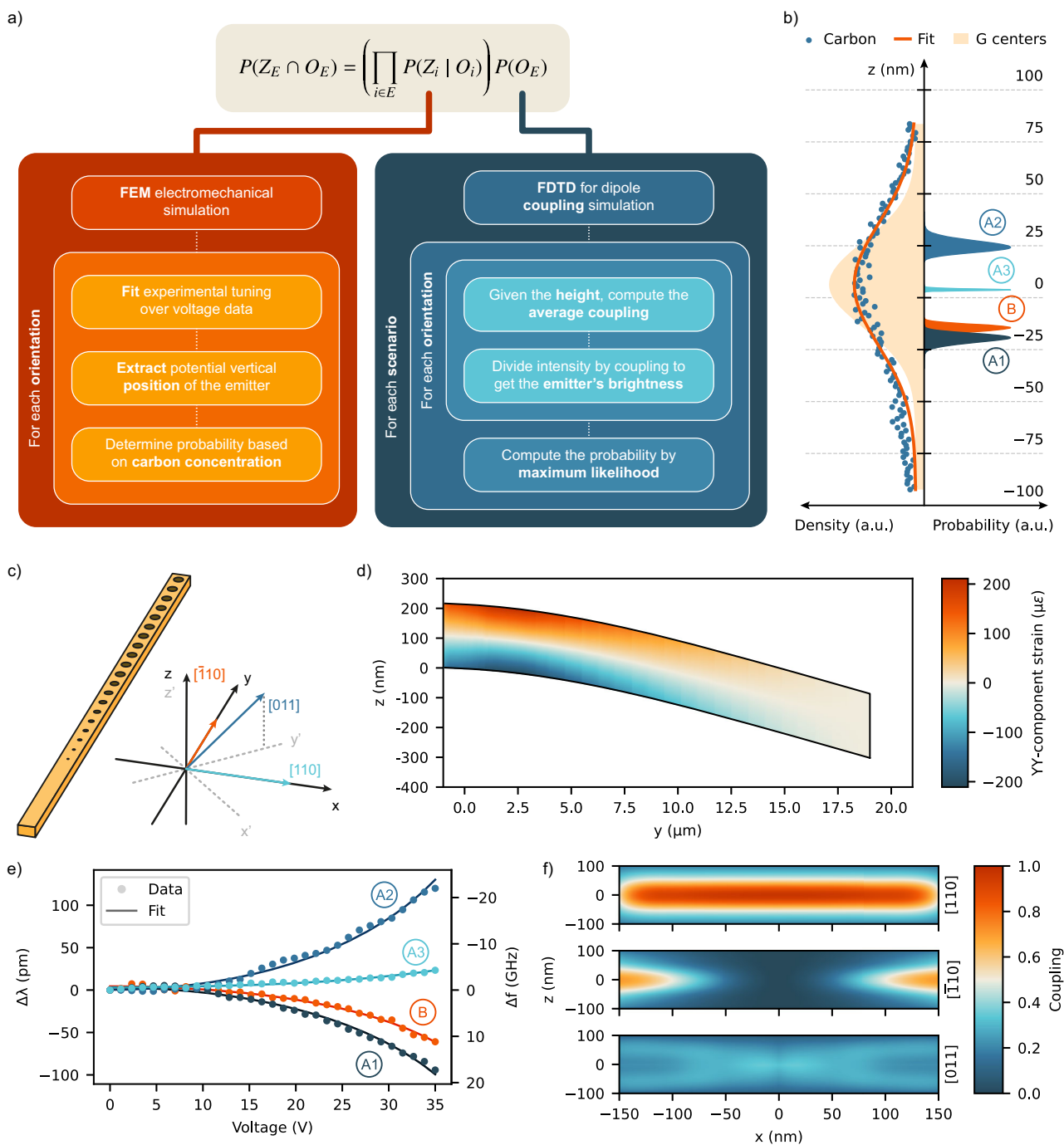


Fig. 4 | Model and simulations for the vertical localization of emitters within the waveguide. **a** Conditional probability model for estimating the vertical localization of the emitters. **b** Comparison of the normalized carbon concentration (orange line) measured via SIMS, with a peak value of 3.3×10^{18} atoms/cm³, and the derived concentration of G-centers (yellow area) within the waveguide, shown on the left, as a function of vertical position within the waveguide. The emitters' vertical localization probability distributions for the most likely scenario are depicted on the right. **c** Schematic of the cantilever waveguide with the coordinate axes used in the analysis. Both the setup framework axis and the crystal framework are shown.

The cantilever is oriented along the $[\bar{1}10]$ direction. **d** Colormap showing the strain distribution along the cantilever and its displacement, extracted from FEM simulations at an applied voltage of 35 V. **e** Spectral shift for four emitters as a function of voltage applied to the cantilever. Dots represent the Lorentzian fit centers of the emission peaks, while the line shows the fitted curve derived from the FEM voltage-strain model used to determine the vertical positions of the emitters. **f** Coupling to the quasi-TE fundamental waveguide mode for three different equivalent classes of emitter orientations as a function of vertical and lateral position in the waveguide.

waveguide cross-section for x and z and at the center of the last tether along the cantilever's y -axis. A three-dimensional finite element method (FEM) simulation calculates the strain versus voltage along the cantilever, with the result at 35 V displayed in Fig. 4d. This simulation reveals the longitudinal strain distribution, which transitions from

compressive to tensile along the vertical axis. To determine the positions of the emitters along the cantilever, we use their y -coordinates extracted from the PL scan in Fig. 3a. Different positions along the cantilever exhibit specific strain profiles, as depicted in the heatmap of Fig. 4d. By fitting the simulated strain curves, evaluated at the PL spot

locations along the cantilever, to the emission wavelength shifts (Fig. 4e), we determine the vertical positions of the emitters associated with each equivalence class of dipole orientations.

We assign probabilities to the positions based on normalized carbon concentration data from secondary ion mass spectroscopy (SIMS), shown in the left plot of Fig. 4b (More details in Supplementary Note 8). Since two carbon atoms and an interstitial silicon are required to form a G-center, assuming a uniform interstitial silicon distribution, the G-center density is quadratic with the carbon concentration. The shaded area in the plot represents this distribution. Consequently, we assign a probability proportional to the square of the normalized carbon concentration at each vertical position. The probabilities for the vertical positions of the color centers, $P(Z_i | O_i)$, are normalized across all possible orientations for each emitter.

The second term of the probability function describes the likelihood of each possible combination of the emitters' dipole orientations, represented by the joint probability of the emitters being aligned along specific directions. To evaluate this probability, we consider the intensity of the color centers' emission and the coupling related to their dipole orientations. The right diagram of Fig. 4a illustrates the corresponding model structure. The measured intensity depends on the excitation power, emitter generation rate, and collection efficiency, which has two components: η_{dip} , the coupling efficiency between the emitter's dipole emission and the waveguide mode, and η_{coll} , the coupling efficiency from the waveguide mode to detection. For the four emitters analyzed, excitation power and η_{coll} are constant, so the main factors influencing intensity are dipole orientations and generation rates. The generation rate, as reported in ref. 16, is assumed to follow a normal distribution. To isolate the impact of the generation rate on the emitters' intensities, the intensity is scaled by dividing it by η_{dip} for each potential scenario. Coupling is averaged across the cantilever's x -direction to account for uniform emitters' distribution. η_{dip} is computed for all dipole orientations and vertical positions via FDTD simulations (Fig. 4f and more details in Supplementary Note 9). Since the dipole coupling to the quasi-TM mode is significantly lower than to the quasi-TE mode (Supplementary Note 9), we only consider the latter one in our model. Once the relative generation rates are obtained, a maximum likelihood estimation determines the most likely Gaussian distribution for these rates. The likelihood of the four-generation rate samples from each distribution is computed, yielding the overall likelihood for each orientation scenario, which corresponds to $P(O_E)$.

We combine the two components of the model to compute the probability for each scenario, evaluating the probability $P(Z_E \cap O_E)$ for all the possible emitter positions and orientations. The distributions, detailed in Supplementary Note 10, show that the most likely scenario (67.0%) corresponds to the case with all emitters aligned along the $[110]$ or $[\bar{1}\bar{1}0]$ direction. Marginal probabilities for these orientations show likelihoods of 98.6%, 96.0%, 93.4%, and 68.2% for emitters B , A_1 , A_2 , and A_3 , respectively. The outcome aligns with our expectation, as the brightest emitters are typically aligned along the $[110]$ direction, making them more likely to be observed during the measurements. Based on these dipole orientations, the vertical positions of the emitters are estimated (right plot of Fig. 4b). Monte Carlo simulations (detailed in Supplementary Note 10) are used to estimate the error in the vertical localization, accounting for uncertainties in FEM simulation, piezospectroscopic coefficients, and y -coordinate positioning. The vertical localization estimate achieves nanometric resolution with error margins below 3 nm.

Discussion

This work tackles key challenges in scaling silicon-based quantum technologies through precise spectral tuning and nanoscale localization of individual color centers. These advancements enable the spectral alignment of multiple color centers, as evidenced by preliminary results demonstrating the tuning of two centers (see

Supplementary Note 7). Furthermore, nanoscale localization facilitates comprehensive studies of local environmental effects on emitter properties, including homogeneous and inhomogeneous spectral distributions. This methodology extends to any type of color center^{28,38–40}, particularly silicon-based defects such as T-centers²⁷ and T-center-like emitters⁴¹, which share the C_{3h} symmetry group with G-centers, thus opening pathways to study and control their optical and spin properties.

Future work should focus on optimizing device design to increase the maximum achievable strain, as detailed in Supplementary Note 11, by reducing cantilever lengths to achieve quadratic strain increase while optimizing the actuation area to maintain low driving voltages. Devices capable of generating larger strains will facilitate the spectral alignment of multiple emitters within a single cantilever and across different devices. These advancements in spectral alignment, when combined with coherent emission, could significantly aid the generation of highly indistinguishable photons, facilitating quantum interference between remote centers for distributed computing¹⁹ and empowering coherent emitter coupling for quantum networks^{42,43}.

By applying multiple strain patterns and experimentally calibrating FEM simulations, nanoscale localization could achieve three-dimensional atomic resolution. This breakthrough would unlock real-time feedback during on-demand emitter generation with local annealing techniques^{44–46} for deterministic generation, precise studies of emitter-cavity coupling, and investigations of local interactions between color centers. Additionally, it could revolutionize quantum sensing by enabling color centers to serve as sensitive probes of local material properties, enhancing our ability to study and control quantum systems at the atomic scale.

In this work, we have demonstrated individual spectral tuning of color centers, characterizing their optical response to strain applied via a MEMS structure integrated into a silicon photonic chip. We have characterized the emitters' optical properties, demonstrating excitation of single color centers, and achieved reversible tuning of individual color centers exceeding 100 pm. This tuning range is sufficient to span the G-centers' inhomogeneous distribution, as reported in ref. 46. Moreover, we have shown that the tuning behavior can be used as a tool to infer the position and orientation of emitters within the waveguide with nanometric precision.

This study establishes a platform for precise control and characterization of color centers in silicon, laying the groundwork for the fundamental understanding of their properties and enabling the development of advanced quantum technologies based on silicon photonics.

Methods

Device design

The photonic integrated circuit is designed on a SOI platform with a nominal device layer thickness of 220 nm. The waveguide width is designed as 350 nm, with a lateral spacing of 2.5 μm between the waveguide and the lateral slab and a 1 μm gap between the cantilever and the slab. The various components of the device were simulated using FDTD simulations with Ansys Lumerical and Tidy3D. The structure consists of a suspended cantilever, terminated by a Bragg reflector, and a waveguide suspended by 10 tethers spaced along a 150 μm length. The tether spacing is defined by a uniform random variable with the center of the distribution set to the maximum value below 20 μm that ensures equal spacing, which in this case is approximately 18 μm . The uniform random component spans a range of 2 μm and is introduced to limit the effects of parasitic Fabry-Perot interference caused by tether scattering. At the end of the waveguide, an inverse linear taper edge coupler is employed to collect light into a fiber. The Bragg reflector, approximately 8 μm long, features 20 holes, 10 for the linear adiabatic transition from the waveguide to the reflector and 10 for the reflector itself, with a hole pitch of 400 nm and a hole radius of

100 nm. The simulated reflectance of the reflector is 95%. The tethers provide mechanical support to the waveguide, keeping it suspended. They are formed by a Gaussian broadening up to a maximum of 720 nm, with a standard deviation of 1.3 μm over a transition length of 4 μm . The simulated transmission is 96% for the quasi-TE mode, with an estimated 94% transmission based on high-resolution micrographs of the fabricated tether structures, as detailed in Supplementary Note 4. The edge coupler is a suspended linear inverse taper with a length of 14 μm and a taper tip width of 110 nm. The simulated transmission efficiency from the waveguide to the UHNA fiber (UHNA3, NA = 0.35) and mode field diameter of 3.3 μm is 59%, with a measured transmission of approximately 12% for the quasi-TE mode at 1280 nm. The cantilever is 20 μm long, with a spacing of 2.0 μm to the ground plane, determined by the buried oxide layer thickness. The cantilever's electromechanical behavior was simulated using the FEM in COMSOL, which resulted in a pull-in voltage of 42.5 V and a maximum strain at pull-in of 510 μe .

Sample fabrication

The fabrication process starts with an SOI wafer with [100] orientation. ^{12}C ions are implanted into the 220 nm device layer using an energy of 36 keV and a fluence of 5×10^{13} ions/cm². RTA is performed at 1000 °C for 20 s in a nitrogen atmosphere to heal the crystalline structure and form G-centers.

Following implantation, the wafer is sent to Applied Nanotools for foundry fabrication. Electron beam (e-beam) lithography is performed using a JEOL JBX8100FS system at 100 kV, patterning the photonic structures. The device layer is etched using a RIE process with SF₆-C₄F₈. A 2 μm thick silicon dioxide (SiO₂) cladding is deposited using PECVD at 300 °C.

Post-processing takes place in the MIT.nano cleanroom. Structures are released by etching the cladding and buried silicon dioxide in a 49% HF solution for 80 s, resulting in an undercut of approximately 2 μm . The chip is transferred from HF to water and then to isopropanol (IPA) while submerged in liquid. CPD is employed using CO₂ to prevent device collapse by gradually replacing the IPA with liquid CO₂. The drying process from liquid CO₂ prevents phase transitions that would otherwise occur during evaporation, thereby avoiding the capillary forces that could cause the suspended structures to collapse. Electrical pads, consisting of 50 nm chromium and 200 nm gold, are patterned using electron beam evaporation (Temescal FC2000) through a shadow mask. The shadow mask is fabricated from a 0.1 mm (4 mil) steel sheet using the LPKF ProtoLaser U4 laser cutter, with 50 μm holes to define the electrical pads. The mask is aligned to the chip under a microscope for alignment with tens of micrometers precision (see Supplementary Note 3 for further details) and held approximately 100 μm above the chip during evaporation. The sample is finally glued with silver paste onto a PCB, and the bonding pads are contacted with an aluminum wire bonder.

Experimental method for spectral tuning and spectroscopy

The bonded sample is mounted in a closed-cycle cryostat (Montana Instrument S50) equipped with an optical window for excitation and fiber-feedthrough for side collection (see Supplementary Note 2). The excitation laser and light source for imaging are directed to the sample through a microscope objective with a numerical aperture of 0.55. Galvanic mirrors are positioned close to the objective to scan the excitation laser position while conserving focus. SNSPDs (Photonspot) optimized for 1550 nm (24% detection efficiency at 1280 nm) are used for low-time jitter (150 ps) detection of single photons, combined with a high time resolution time tagger (Swabian Instruments Timetagger 20). Spectra are recorded on an Oxford Instrument spectrometer equipped with a nitrogen-cooled camera (Pylon IR CCD) with an integration time of 60 s and 1% detection efficiency at 1280 nm. DC voltage is applied through a voltage source (Keithley 2400), and

upward and downward sweeps are recorded. Photoluminescence emitted in the waveguide mode is collected with the UHNA3 fiber.

Photoluminescence raster maps. The PL maps presented in Fig. 3a are obtained by triggering the recording of photon counts on a time tagger channel by the voltage applied on the galvanic mirrors, with an integration time of 100 ms. In this case, the collected emission is filtered through a free-space filter (1250–1300 nm) of 60% efficiency to remove background luminescence from the signal and then fiber-coupled to a single SNSPD.

Second-order correlation function and lifetime. To isolate a single ZPL, the collected emission is sent to a fiber-based tunable narrowband filter (WL Photonics) with a 0.1 nm bandwidth, combined with a wavelength demultiplexer with output at 1280 nm for suppressing background light. The filtered ZPL is then coupled to a 50:50 fiber-based beam splitter, whose outputs are coupled to two SNSPDs. The function used to fit the normalized correlation reads

$$g^{(2)}(\tau) = (1 - Ae^{-|\tau|/\tau_a}) \cdot (1 + Be^{-|\tau|/\tau_b}), \quad (3)$$

where A and B are the antibunching and bunching coefficients, respectively, associated with corresponding time constants τ_a and τ_b . From a non-linear least squares fitting method, we extract an antibunching constant of $A = 0.98 \pm 0.09$ with a fixed bunching constant of $B = 1.56$.

For the time-resolved measurement, we switch the excitation laser to a pulsed broadband laser (SuperK, NKT Photonics) equipped with a tunable bandwidth filter, which we center at 532 nm. The lifetime is then fitted to a mono-exponential as

$$I(t) = e^{-t/\tau} + c, \quad (4)$$

for $t > t_0$, where c accounts for the constant background and τ is the total lifetime of the G-center, containing both radiative and non-radiative decays.

Saturation of a two-level system. Emission into the ZPL as a function of excitation power is recorded by coupling the collected photons to the spectrometer, without additional filtering. The ZPL peaks are then integrated and fitted to

$$I_{\text{int}}(P) = I_{\text{max}} \frac{P}{P + P_{\text{sat}}} \quad (5)$$

to extract the saturation power.

Nanoscale localization model

Piezospectroscopic model. The G-center is characterized by two substitutional carbon atoms bonded to an interstitial silicon atom Si_{int}. Through experimental studies⁴⁷ and first-principles analysis³⁴, it has been confirmed that the defect exhibits monoclinic- C_{2h} symmetry and behaves as a linear π oscillator perpendicular to the symmetry plane. The C-C bond can be oriented along four equivalent crystal directions: [111], $[\bar{1}\bar{1}\bar{1}]$, $[1\bar{1}\bar{1}]$, $[\bar{1}\bar{1}1]$. Additionally, the Si_{int} atom can occupy six possible configurations around the C-C bond. Due to the low symmetry of this defect, the multiplicity of orientational degeneracy is 24, from the ratio between the orders of the crystal symmetry group O_h for silicon and of the center of the defect, representing the number of possible equivalent orientations inside the crystal.

Under external stress, the energy transitions shift for a non-cubic point group in a cubic crystal can be expressed using the equation

$$\Delta E = \sum_{i,j=x,y,z} A_{ij} \sigma_{ij}^{\text{ext}}, \quad (6)$$

where ΔE corresponds to the energy shift for the identity orientation in the crystal coordinate system, the A_{ij} coefficients form a second-rank symmetric tensor, and σ_{ij}^{ext} represents the external stress components. Once the symmetry of the defect is established, this expression can be reformulated using the piezospectroscopic model developed for non-cubic defects in cubic crystals⁴⁸. In this model, a matrix A_p is associated with the stress tensor. For a monoclinic-I defect with a plane aligned along (110), A_p assumes the following shape

$$A_p = \begin{pmatrix} A_2 & A_3 & -A_4 \\ A_3 & A_2 & A_4 \\ -A_4 & A_4 & A_1 \end{pmatrix}. \quad (7)$$

By performing the matrix product with the stress tensor, the derived final expression is

$$\Delta E = A_1 \sigma_{zz}^{\text{ext}} + A_2 (\sigma_{xx}^{\text{ext}} + \sigma_{yy}^{\text{ext}}) + 2A_3 \sigma_{xy}^{\text{ext}} + 2A_4 (\sigma_{yz}^{\text{ext}} - \sigma_{zx}^{\text{ext}}). \quad (8)$$

Applying uniaxial strain along a specific crystal direction breaks the symmetry of the defect and lifts the orientational degeneracy, resulting in an energy splitting. The number of splits depends on the direction of the applied strain. For a strain applied along the $\overline{[110]}$ direction, the nonzero components of the strain tensor in crystal coordinates are ϵ_{xx} , ϵ_{yy} , ϵ_{xy} , with an additional ϵ_{zz} component arising from Poisson's ratio of silicon (see Supplementary Note 12). Using FEM analysis, the magnitude of the applied uniaxial strain in the cantilever can be calculated, and the corresponding strain tensor in crystal coordinates can be determined. The A_i coefficients are obtained from previous experimental studies³⁶, and the terms of the elastic matrix of silicon can be used to compute the strain-stress conversion. By applying the piezospectroscopic model and accounting for all possible defect rotations for a monoclinic-I symmetry, four distinct shift rates can be identified, depending on the orientation of the defect within the crystal (see Supplementary Note 13).

Localization error by Monte Carlo simulation. The error in the vertical localization of the emitters is assessed through Monte Carlo simulations and arises from three primary sources of uncertainty: the estimation of the position along the cantilever (y -direction), the accuracy of the FEM simulation of maximum strain values, and the variability in the piezospectroscopic model constants. For emitters located at spot A and spot B (as shown in Fig. 3a), the uncertainty in the y -direction accounts for errors in the positioning and size of the excitation laser spot. Standard deviations of 500 nm and 750 nm are used for the positions of spots A and B , respectively, with spot B exhibiting higher uncertainty due to its farther distance from the tether and the resulting less precise positioning along the cantilever. These values approximately correspond to twice the size of the diffraction-limited spot. A 20% uncertainty is applied to the FEM maximum strain values, based on literature estimates⁴⁹. The variability in the piezospectroscopic constant is quantified using the sample standard deviation of literature values^{36,37}, resulting in a 4.7% error. All sources of uncertainty are modeled as Gaussian noise in the Monte Carlo simulations. The results of these simulations are displayed in Supplementary Note 10.

G-centers concentration. To estimate the relationship between carbon concentration and G-centers' formation, we model the density of

G-centers using a rate equation that accounts for the reactants involved in their formation. The G-center is formed by two substitutional carbon atoms (C_{sub}) and one interstitial silicon atom (Si_{int}). The rate equation for the concentration of G-centers, denoted as $[G]$, is given by

$$[G] = k \cdot [C_{\text{sub}}]^2 \cdot [Si_{\text{int}}], \quad (9)$$

where k is the formation efficiency, $[C_{\text{sub}}]$ is the concentration of substitutional carbon atoms, and $[Si_{\text{int}}]$ is the concentration of interstitial silicon atoms. Assuming the concentration of substitutional carbon atoms linearly proportional to the overall carbon concentration $[C]$ and the concentration of interstitial silicon to be constant within the waveguide, the G-center concentration will depend quadratically from the carbon concentration, such that $[G] \propto [C]^2$.

Conditional probability factorization. The term $P(Z_E | O_E)$ is factorized under the assumption of marginal independence of emitter positions given their orientations. The assumption means that conditioned on their orientations, the position of one emitter is independent of the positions and orientations of the other emitters, leading to

$$P(Z_E | O_E) = \prod_{i \in E} P(Z_i | O_i), \quad (10)$$

where $P(Z_i | O_i)$ is the probability that emitter i is at position z_i , given that its orientation belongs to the equivalence class O_i . The factorization relies on two assumptions: (1) the positions of emitters are independent given their orientations, i.e., for $i \neq j$, $P(Z_i, Z_j | O_E) = P(Z_i | O_E) P(Z_j | O_E)$; and (2) the position of an emitter is independent of the orientations of other emitters, implying $P(Z_i | O_E) = P(Z_i | O_i)$.

Data availability

All datasets supporting the findings of this study, sufficient to reproduce the plots and analyses in the manuscript, are available on Zenodo under <https://doi.org/10.5281/zenodo.16989979>.

Code availability

The analysis code and Jupyter notebooks required to process the data and generate the figures in this study are available at <https://doi.org/10.5281/zenodo.16989979>.

References

- Aharonovich, I., Englund, D. & Toth, M. Solid-state single-photon emitters. *Nat. Photonics* **10**, 631–641 (2016).
- Awschalom, D. D., Hanson, R., Wrachtrup, J. & Zhou, B. B. Quantum technologies with optically interfaced solid-state spins. *Nat. Photonics* **12**, 516–527 (2018).
- Bhaskar, M. K. et al. Experimental demonstration of memory-enhanced quantum communication. *Nature* **580**, 60–64 (2020).
- Pompili, M. et al. Realization of a multinode quantum network of remote solid-state qubits. *Science* **372**, 259–264 (2021).
- Knaub, C. M. et al. Entanglement of nanophotonic quantum memory nodes in a telecom network. *Nature* **629**, 573–578 (2024).
- Randall, J. et al. Many-body-localized discrete time crystal with a programmable spin-based quantum simulator. *Science* **374**, 1474–1478 (2021).
- Choi, H., Pant, M., Guha, S. & Englund, D. Percolation-based architecture for cluster state creation using photon-mediated entanglement between atomic memories. *npj Quantum Inf.* **5**, 1–7 (2019).
- Redjem, W. et al. Single artificial atoms in silicon emitting at telecom wavelengths. *Nat. Electron.* **3**, 738–743 (2020).
- Higginbottom, D. B. et al. Optical observation of single spins in silicon. *Nature* **607**, 266–270 (2022).

10. Atabaki, A. H. et al. Integrating photonics with silicon nanoelectronics for the next generation of systems on a chip. *Nature* **556**, 349–354 (2018).
11. Saggio, V. et al. Cavity-enhanced single artificial atoms in silicon. *Nat. Commun.* **15**, 5296 (2024).
12. Redjem, W. et al. All-silicon quantum light source by embedding an atomic emissive center in a nanophotonic cavity. *Nat. Commun.* **14**, 3321 (2023).
13. Islam, F. et al. Cavity-enhanced emission from a silicon t center. *Nano Lett.* **24**, 319–325 (2024).
14. Johnston, A., Felix-Rendon, U., Wong, Y.-E. & Chen, S. Cavity-coupled telecom atomic source in silicon. *Nat. Commun.* **15**, 2350 (2024).
15. Lee, C.-M. et al. High-efficiency single photon emission from a silicon T-center in a nanobeam. *ACS Photonics* **10**, 3844–3849 (2023).
16. Prabhu, M. et al. Individually addressable and spectrally programmable artificial atoms in silicon photonics. *Nat. Commun.* **14**, 2380 (2023).
17. Komza, L. et al. Indistinguishable photons from an artificial atom in silicon photonics. *Nat. Commun.* **15**, 6920 (2024).
18. Simmons, S. Scalable fault-tolerant quantum technologies with silicon color centers. *PRX Quantum* **5**, 010102 (2024).
19. Afzal, F. et al. Distributed quantum computing in silicon. Preprint at <http://arxiv.org/abs/2406.01704> (2024).
20. Li, L. et al. Heterogeneous integration of spin-photon interfaces with a CMOS platform. *Nature* **630**, 70–76 (2024).
21. Papon, C. et al. Independent operation of two waveguide-integrated quantum emitters. *Phys. Rev. Appl.* **19**, L061003 (2023).
22. Chu, X.-L. et al. Independent electrical control of two quantum dots coupled through a photonic-crystal waveguide. *Phys. Rev. Lett.* **131**, 033606 (2023).
23. Larocque, H. et al. Tunable quantum emitters on large-scale foundry silicon photonics. *Nat. Commun.* **15**, 5781 (2024).
24. Ristori, A. et al. Strain engineering of the electronic states of silicon-based quantum emitters. *Adv. Opt. Mater.* 2301608. <https://onlinelibrary.wiley.com/doi/abs/10.1002/adom.202301608> (2023).
25. Durand, A. et al. Hopping of the center-of-mass of single G centers in silicon-on-insulator. *Phys. Rev. X* **14**, 041071 (2024).
26. Day, A. M. et al. Electrical manipulation of telecom color centers in silicon. *Nat. Commun.* **15**, 4722 (2024).
27. Clear, C. et al. Optical transition parameters of the silicon T centre. *Phys. Rev. Appl.* **22**, 064014 (2024).
28. Meesala, S. et al. Strain engineering of the silicon-vacancy center in diamond. *Phys. Rev. B* **97**, 205444 (2018).
29. Sohn, Y.-I. et al. Controlling the coherence of a diamond spin qubit through its strain environment. *Nat. Commun.* **9**, 2012 (2018).
30. Machielse, B. et al. Quantum interference of electromechanically stabilized emitters in nanophotonic devices. *Phys. Rev. X* **9**, 031022 (2019).
31. Brevoord, J. M. et al. Large-range tuning and stabilization of the optical transition of diamond tin-vacancy centers by in-situ strain control. *Appl. Phys. Lett.* **126**, 174001 (2025).
32. Rengstl, U. et al. On-chip beamsplitter operation on single photons from quasi-resonantly excited quantum dots embedded in GaAs rib waveguides. *Appl. Phys. Lett.* **107**, 021101 (2015).
33. Davanço, M., Hellberg, C. S., Ates, S., Badolato, A. & Srinivasan, K. Multiple time scale blinking in InAs quantum dot single-photon sources. *Phys. Rev. B* **89**, 161303 (2014).
34. Udvarhelyi, P., Somogyi, B., Thiering, G. & Gali, A. Identification of a telecom wavelength single photon emitter in silicon. *Phys. Rev. Lett.* **127**, 196402 (2021).
35. Durand, A. et al. Genuine and faux single G centers in carbon-implanted silicon. *Phys. Rev. B* **110**, L020102 (2024).
36. Foy, C. P., Carmo, M. C. D., Davies, G. & Lightowers, E. C. Uniaxial stress measurements on the 0.97 eV line in irradiated silicon. *J. Phys. C Solid State Phys.* **14**, L7 (1981).
37. Davies, G., Lightowers, E. C. & Carmo, M. D. Carbon-related vibronic bands in electron-irradiated silicon. *J. Phys. C Solid State Phys.* **16**, 5503 (1983).
38. Lukin, D. M. et al. 4H-silicon-carbide-on-insulator for integrated quantum and nonlinear photonics. *Nat. Photonics* **14**, 330–334 (2020).
39. Bourassa, A. et al. Entanglement and control of single nuclear spins in isotopically engineered silicon carbide. *Nat. Mater.* **19**, 1319–1325 (2020).
40. Sarihan, M. C. et al. Photophysics of O-band and transition metal color centers in monolithic silicon for quantum communications. *Commun. Phys.* **8**, 1–11 (2025).
41. Xiong, Y. et al. Computationally driven discovery of T center-like quantum defects in silicon. *J. Am. Chem. Soc.* **146**, 30046–30056 (2024).
42. Sipahigil, A. et al. An integrated diamond nanophotonics platform for quantum-optical networks. *Science* **354**, 847–850 (2016).
43. Tiranov, A. et al. Collective super- and subradiant dynamics between distant optical quantum emitters. *Science* **379**, 389–393 (2023).
44. Hollenbach, M. et al. Wafer-scale nanofabrication of telecom single-photon emitters in silicon. *Nat. Commun.* **13**, 7683 (2022).
45. Jhuria, K. et al. Programmable quantum emitter formation in silicon. *Nat. Commun.* **15**, 4497 (2024).
46. Gu, Q. et al. End-to-end physics-based modeling of laser-activated color centers in silicon. Preprint at <http://arxiv.org/abs/2501.17240> (2025).
47. Thonke, K., Klemisch, H., Weber, J. & Sauer, R. New model of the irradiation-induced 0.97-eV (G) line in silicon: a C_s-Si* complex. *Phys. Rev. B* **24**, 5874–5886 (1981).
48. Kaplyanskii, A. A. Noncubic centers in cubic crystals and their spectra in external fields. *J. Phys. Colloq.* **28**, C4–48 (1967).
49. Song, J., Huang, Q.-A., Li, M. & Tang, J.-Y. Effect of die-bonding process on MEMS device performance: system-level modeling and experimental verification. *J. Microelectromech. Syst.* **18**, 274–286 (2009).
50. O'Donnell, K. P., Lee, K. M. & Watkins, G. D. Origin of the 0.97 eV luminescence in irradiated silicon. *Phys. B+C* **116**, 258–263 (1983).

Acknowledgements

The authors acknowledge S. Nagle for assisting with the fabrication of the holder and mask for the shadow-mask evaporation and I. Christen for manufacturing the fiber holder for the cryostat, providing laboratory support, and contributing to valuable discussions. The authors also acknowledge S. Gyger and H. Larocque's contributions to the simulations during the early-stage design. I. Berkman is acknowledged for proofreading the manuscript and offering constructive feedback. Finally, the authors thank S. Patomäki for assistance with the chip wire bonding. This work was supported by the NSF Convergence Accelerator program (Award No. 2134891). C.P. acknowledges support from the NSF Engineering Research Center for Quantum Networks (Co-operative Agreement No. 1941583). M.P. and C.E.-H. acknowledge financial support from the Dutch Research Council (Project No. NGF.1623.23.027). V.S. acknowledges support from the Air Force Office of Scientific Research (AFOSR) under Award No. GR108261. D.E. acknowledges support from the NSF RAISE TAQS program. This material is based on research sponsored by the Air Force Research Laboratory (AFRL), under agreement number FA8750-20-2-1007. The U.S. Government is authorized to reproduce and distribute reprints for Governmental purposes, notwithstanding any copyright notation thereon. The views and conclusions contained herein are those of the authors and should not be

interpreted as necessarily representing the official policies or endorsements, either expressed or implied, of the Air Force Research Laboratory (AFRL) or the U.S. Government.

Author contributions

A.B. and C.E.-H. conceptualized the device. A.B., C.E.-H., and H.R. conducted simulations and design work, while A.B. was responsible for the chip layout. The preprocessing of fabrication was carried out by A.B. and C.E.-H., with post-processing by A.B. and C.P. Experimental characterization and data analysis were performed by C.P. and A.B., with support from O.H. and V.S. The physical model for nanoscale localization was developed by A.B., in collaboration with M.P. for the piezospectroscopic model and C.P. for the color center coupling. C.E.-H., V.S., and D.E. supervised the work. All authors contributed to the writing of the manuscript.

Competing interests

The authors declare no competing interests.

Additional information

Supplementary information The online version contains supplementary material available at <https://doi.org/10.1038/s41467-025-63871-8>.

Correspondence and requests for materials should be addressed to Alessandro Buzzi, Camille Papon, Carlos Errando-Herranz or Dirk Englund.

Peer review information *Nature Communications* thanks the anonymous reviewers for their contribution to the peer review of this work. A peer review file is available.

Reprints and permissions information is available at <http://www.nature.com/reprints>

Publisher's note Springer Nature remains neutral with regard to jurisdictional claims in published maps and institutional affiliations.

Open Access This article is licensed under a Creative Commons Attribution-NonCommercial-NoDerivatives 4.0 International License, which permits any non-commercial use, sharing, distribution and reproduction in any medium or format, as long as you give appropriate credit to the original author(s) and the source, provide a link to the Creative Commons licence, and indicate if you modified the licensed material. You do not have permission under this licence to share adapted material derived from this article or parts of it. The images or other third party material in this article are included in the article's Creative Commons licence, unless indicated otherwise in a credit line to the material. If material is not included in the article's Creative Commons licence and your intended use is not permitted by statutory regulation or exceeds the permitted use, you will need to obtain permission directly from the copyright holder. To view a copy of this licence, visit <http://creativecommons.org/licenses/by-nc-nd/4.0/>.

© The Author(s) 2025